

Kinematics of the gas in a barred galaxy: do strong shocks inhibit star formation?

D. Reynaud and D. Downes

Institut de Radio Astronomie Millimétrique, F-38406 Saint Martin d'Hères, France

Received 11 May 1998 / Accepted 17 June 1998

Abstract. We present new CO(1–0) maps of the barred spiral galaxy NGC 1530 with a resolution of $5''.3$, obtained by adding short spacing visibilities from the IRAM 30m telescope to data from the IRAM interferometer. The improvement in sensitivity is spectacular, allowing us to detect with high signal-to-noise the extended CO lanes along the bar of the galaxy. These molecular gas lanes, which are density waves or shocks created by the barred potential, show a remarkable kinematic pattern. We find 50 to 100 km s^{-1} outward motions upstream of the lanes, and 70 to 150 km s^{-1} inward motions in and downstream of the lanes. The intensity of the shocks is greatest near the central CO concentration, and decreases to zero at the ends of the bar. We compare these kinematic features with a map of the $\text{H}\alpha$ distribution that traces young stars. Star formation is very intense around the nucleus of the galaxy and at the ends of the bar. It is weak halfway between these extremities. In general, the HII regions are downstream of the CO lanes. The star formation is probably inhibited in the lanes at the places where the shocks and the shear are too strong. There may be a maximum threshold of 80 to 170 km s^{-1} for the relative velocity of any cloud entering the density wave, above which the cloud cannot form stars.

Key words: galaxies: structure – galaxies: individual: NGC 1530 – galaxies: ISM – galaxies: kinematics and dynamics – radio lines: galaxies

1. Introduction

Bars are important in the evolution of spiral galaxies because they can bring huge quantities of dense molecular gas into galactic centers. The barred potential induces a net inflow of gas in galactic disks through the torque of the bar on the interstellar gas and through the formation of intense dissipative shocks (e.g., Roberts et al. 1979; Combes 1988). These shocks are associated with straight dust lanes that are offset from the bar's major axis. The shape of these shocks is well reproduced by hydrodynamic simulations, which indicate that the shocks provoke an infall of the gas into the center of the galaxy, with an

average infall velocity of 1 km s^{-1} (e.g. Athanassoula 1992). From smoothed-particle-hydrodynamic simulations, the infall rate has been estimated to be $0.2 - 7 M_{\odot} \text{ yr}^{-1}$, with accretion peaks up to $100 M_{\odot} \text{ yr}^{-1}$ (Friedli & Benz 1993). This rate may be able to feed the activity of starburst galaxies and moderate AGNs.

Roberts et al. (1979) showed from 1D simulations that the dust lanes occur at the locations of hydrodynamic shocks, with a discontinuity of the velocity component perpendicular to the shock fronts (in a reference frame rotating with the bar). The velocity component tangent to the shock front has a continuous gradient at the crossing of the shock that varies from an outward motion of $+120 \text{ km s}^{-1}$ (upstream) to an inward motion of -125 km s^{-1} (in and downstream of the shock). The 2D simulations of Athanassoula (1992) confirm these results giving a value of 100 to 300 pc for the scale length of the velocity gradient in a “standard” barred galaxy.

Observers have detected these velocity jumps associated with the dust lanes. For a review on this subject, see Athanassoula (1992). For example, in the SABc galaxy NGC 6221, Pence & Blackman (1984) detected in $\text{H}\alpha$ data a velocity jump of 150 km s^{-1} over a distance $\leq 300 \text{ pc}$. This velocity jump is the transition from outward to inward motion predicted by the hydrodynamic models. The entire bar in that galaxy was not studied, as the authors used slits at discrete positions along the bar. There remains a need to study the kinematics of the interstellar gas in barred galaxies, with full sampling. This was the aim of our study of NGC 1530 in CO, which also has the advantage of not being confused by dust extinction.

The dust and CO lanes along galactic bars are the tracers of a shock wave similar to the density waves of spiral arms in galaxy disks, but with much higher velocity gradients. One expects to find in the bars HII regions offset from the CO arms, just as in the spiral arms of galaxies. This is not always the case. While late-type barred galaxies frequently show a lane of HII regions aligned with the major axis of the bar, early-type barred galaxies show almost no star formation along the bar, except in the nuclear region of the galaxy and at the ends of the bar (Phillips 1996). The explanation for this is still not clear, but our CO(1–0) observations suggest that the star formation is possibly inhibited by the strong shear and shock in the interstellar gas due to the barred potential.

Send offprint requests to: D. Reynaud, (reynaud@iram.fr)

We have focused our study on NGC 1530, a typical barred galaxy of type SBb (early-type). Two straight absorbing dust lanes are visible along the bar. These bands are initially curved¹ and then run straight from the nucleus to the ends of the bar, as can be seen in the reddening maps (B–K, V–K) published by Regan et al. (1995).

Radio continuum observations at 1.4 GHz, with $\simeq 15''$ resolution, show an intense central component and emission along the bar out to the beginning of the spiral arms (Condon et al. 1996; Regan et al. 1996). This is the synchrotron radiation from relativistic particles in the magnetic field that is enhanced by the bar shocks. NGC 1530 was also mapped in HI (30'' resolution) and H α (4'' resolution) (Regan et al. 1996). The HI is confined to the spiral arms, and is absent in the bar. H α is found mainly in the nuclear zone, *along the dust lanes* (unlike many other early-type barred galaxies) and in the spiral arms. From the H α velocity map, Regan et al. (1997) modeled the galaxy dynamics and calculated an accretion rate of $1 M_{\odot} \text{ yr}^{-1}$ in the nuclear ring of NGC 1530. Shocks in the interstellar gas must have given birth to massive stars with the HII regions along the dust lanes and inside the nucleus.

Regan et al. (1995) mapped CO(1–0) in this galaxy with the BIMA interferometer and the NRAO 12m telescope (for the short spacings), at 5'' resolution. Because of the limited sensitivity, they detected the central CO concentration and a few clouds at the ends of the bar. Downes et al. (1996) showed CO observations of NGC 1530 along the bar, made at the IRAM interferometer with a 3.7'' resolution, *without* the short spacing visibilities. Although the extended CO lanes were detected, nicely superimposed on the dust lanes, the missing flux from the extended structures made it difficult to do a very precise analysis.

In this paper, we report the observations with the IRAM 30m telescope that provide short spacing data in CO(1–0) along the entire bar, allowing a better analysis of the kinematics of the gas.

2. Observations, data reduction

Our CO(1–0) interferometer observations were originally made in 1993–1994 with the IRAM Interferometer on Plateau de Bure, France, with four 15m antennas. The bar of NGC 1530 was observed in a mosaic of five partially overlapping fields, with projected baselines from 20m to 180m, with a channel width of 20 km s^{-1} . The data reduction is described in Downes et al. (1996).

To add the visibilities at short spacings, we observed the galaxy with the IRAM 30m telescope in June and November 1996. The bar was mapped on a grid with a 7'' step, to oversample the 21'' beam. We used two receivers at 3mm, followed by two $512 \times 1 \text{ MHz}$ filter banks. The receiver noise temperatures were 100 and 150 K, and the system temperatures were 330 and 350 K (in T_{A}^* units). The response of the 30m telescope

is $6.3 \text{ Jy K}_{T_{\text{A}}}^{-1}$ at 114 GHz. The observations were made with a secondary wobbling at 0.5 Hz, with a beam throw of $240''$. Each position was observed for 8 minutes. The pointing was checked every 20 min. For the first period (June 1996) the two receivers were aligned with an accuracy of $2''$ which allowed us to combine them and to reduce the noise in the spectra by a factor of $\sqrt{2}$. For the second period (November 1996) the two receivers were depointed by $4''$ so we eliminated the scans of the less sensitive receiver.

In the data reduction, we subtracted a baseline for each scan and eliminated bad channels by linear interpolation between adjacent channels. We then added the spectra taken at the same positions, and obtained a set of spectra covering the entire region mapped by the interferometer. From this set of spectra we made CO maps in 20 km s^{-1} wide channels. We then calculated the short spacing visibilities from these maps by correcting for the beam of the 30m telescope and simulating the primary beam of the 15m telescopes, for the five fields mapped by the interferometer. We then merged the resulting tables of visibilities with the ones produced by the interferometer. From these five tables we produced 20 km s^{-1} channel maps by Fourier transform and deconvolution by the algorithm of Clark (1980) adapted for the special case of mosaics (Viallefond et al. 1994). Then we calculated the integrated intensity maps by summing the channel maps with an integration threshold of 2σ .

For the interferometer visibilities, each data point was weighted by T_{sys}^{-2} where T_{sys} is the geometric mean system temperature of the antenna pairs. For the 30m visibilities, the parameter controlling their total weight (W) was chosen by iteration. For too weak a value of W , one obtains the same maps as with the array alone, with no gain in flux. For too high a value, the beam size is increased, losing the advantage of the high resolution of the interferometer.

We obtained an optimum compromise between sensitivity and resolution with $W = 6.6 \times 10^{-4}$. This gave a $5''.6 \times 5''.0$ beam at p. a. -15° . The beam is only slightly larger than the one obtained with the array alone ($3''.9 \times 3''.5$). The total flux measured in the bar of NGC 1530 with this weight is 550 Jy km s^{-1} , which is 90% of the total flux measured with the 30m alone (622 Jy km s^{-1}). The total flux measured with the interferometer alone is 400 Jy km s^{-1} , so 36% of the total flux from the bar is lost by the interferometer due to the missing short spacings.

3. Results

Fig. 1a and b shows a comparison of the integrated intensity map from the array alone convolved to $5''.3$, with the integrated intensity map from the array data combined with the 30m data ($W = 6.6 \times 10^{-4}$, resolution $5''.3$. The combined Plateau de Bure plus Pico Veleta maps are hereafter called PdB+PV). The gain obtained by adding the short spacing data is spectacular: elongated CO lanes are detected all along the bar from the center out to the beginning of the spiral arms (north-west and south-east corners of the mosaic). In the map from the array alone, the CO lanes are weaker and less regular. The noise in the individual channel maps is also higher due to the missing short spacing vis-

¹ see the arcs limiting the central plateau north and south of the nucleus in Reynaud & Downes (1997).

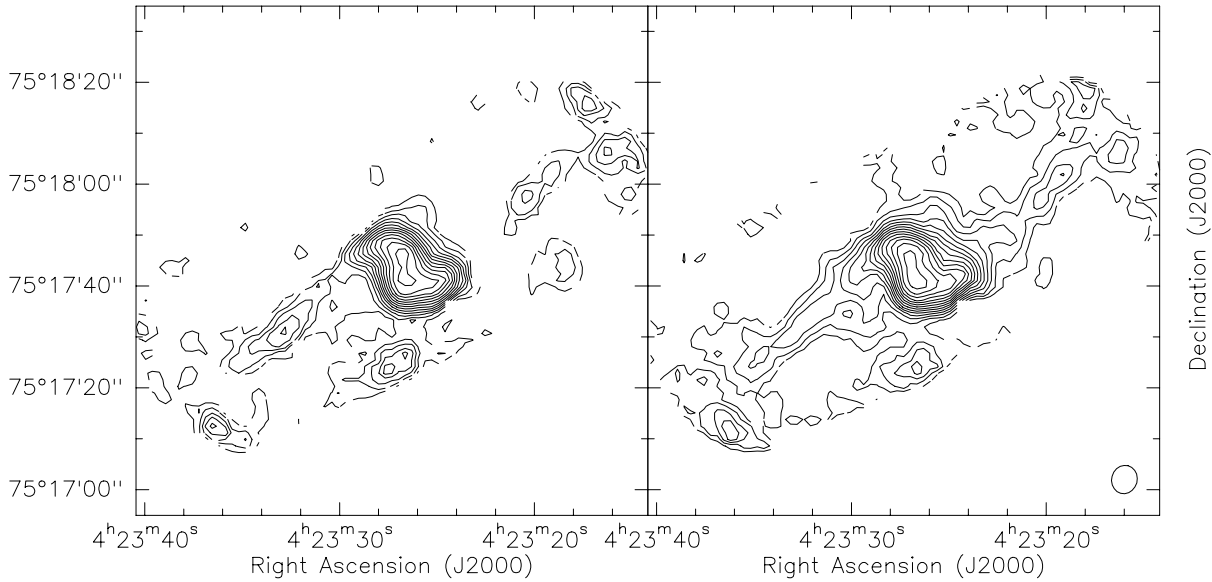


Fig. 1a and b. Comparison of integrated CO maps along the bar of NGC 1530. **a** left: array data without short spacings; **b** right: array data with short spacings. Contours are the same in both figures ($3 \text{ Jy beam}^{-1} \text{ km s}^{-1}$). The clean beam (ellipse at the bottom-right), is $5''.3$ for both maps.

ibilities (17 mJy beam^{-1} instead of 10 mJy beam^{-1}). The noise in the integrated map (PdB+PV) is $\sigma = 1 \text{ Jy beam}^{-1} \text{ km s}^{-1}$. We use these PdB+PV maps as best showing the weak extended features that are the subject of this paper.

Fig. 2 shows the 20 km s^{-1} wide channel maps of the mosaic PdB+PV. The CO bar is well detected in the channels from 2430 to 2490 km s^{-1} , with a Z shape indicating non-circular motions (see below).

4. Molecular gas distribution

Fig. 3 shows the integrated CO map done with PdB+PV superimposed on an optical image of the bar and the inner part of the spiral arms of NGC 1530. The CO map shows many interesting features, including:

- An intense central plateau in the form of a Z, with two curved arms connected to the extended CO lanes. This central plateau has been studied extensively at high resolution ($1.8''$) (Reynaud & Downes 1997). The total flux of this central plateau is 362 Jy km s^{-1} in the PdB+PV map.
- Two extended narrow lanes of molecular gas that coincide with the dust absorption lanes in the optical image. These lanes run along each side of the central plateau, and continue along the bar until the beginning of the main spiral arms (Fig. 3). These lanes are shifted toward the leading side of the bar, as is usual in barred galaxies with straight dust lanes (Athanasoula 1992). The eastern lane is more regular than the western one, which has alternating CO clumps and voids (see the zone near the central plateau at the west). Although the CO distribution is more regular than was suggested by the interferometer alone map or by optical images, the CO lanes on the new map remain rather asymmetric.

- There are large concentrations of molecular gas at the west end of the bar, where the spiral arm begins. The end of the east arm is different, with a void between the end of the lane and the beginning of the spiral arm. The spiral arm is detected in the CO mosaic, but is truncated by the primary beam.
- There is a large clump of gas $20''$ south of the center of NGC 1530. This very large molecular complex is at the edge of the mosaic, where the noise is high. In the visible opacity map published by Regan et al. (1995), there is a large dust complex at the same place as the molecular gas complex.
- There is weak and diffuse CO(1–0) emission at the southern edge of the east lane and the northern edge of the west lane. The detections are at the 4σ level ($4 \text{ Jy beam}^{-1} \text{ km s}^{-1}$).

We compared our CO map with that made by Regan et al. (1995) with a $4''.8$ beam with the BIMA interferometer and the NRAO 12m (for the short spacings). This CO map (Fig. 2 of Regan et al. 1995) shows the central plateau and a few CO clumps at the ends of the CO lanes. But it does not show the CO lanes themselves, nor the CO concentration that we find $20''$ south of the center of NGC 1530. When convolved to the same resolution as ours, the BIMA+NRAO 12m image has an r.m.s. noise of $\sigma \simeq 3 \text{ Jy beam}^{-1} \text{ km s}^{-1}$, three times poorer than ours ($\sigma \simeq 1 \text{ Jy beam}^{-1} \text{ km s}^{-1}$). This explains their non-detection of the weak CO lanes, which have an average brightness of $\simeq 8 \text{ Jy beam}^{-1} \text{ km s}^{-1}$.

The same authors mapped the optical depth of the dust (Fig. 7a of Regan et al. 1995 inverted with Fig. 8) from images in the visible and near-IR in the B, V, R, I, J, H and K bands, and from a model of multiple diffusion of the light on the dust grains. This opacity map has a resolution of $1''.7$, and shows the same features as our CO maps. The intense cen-

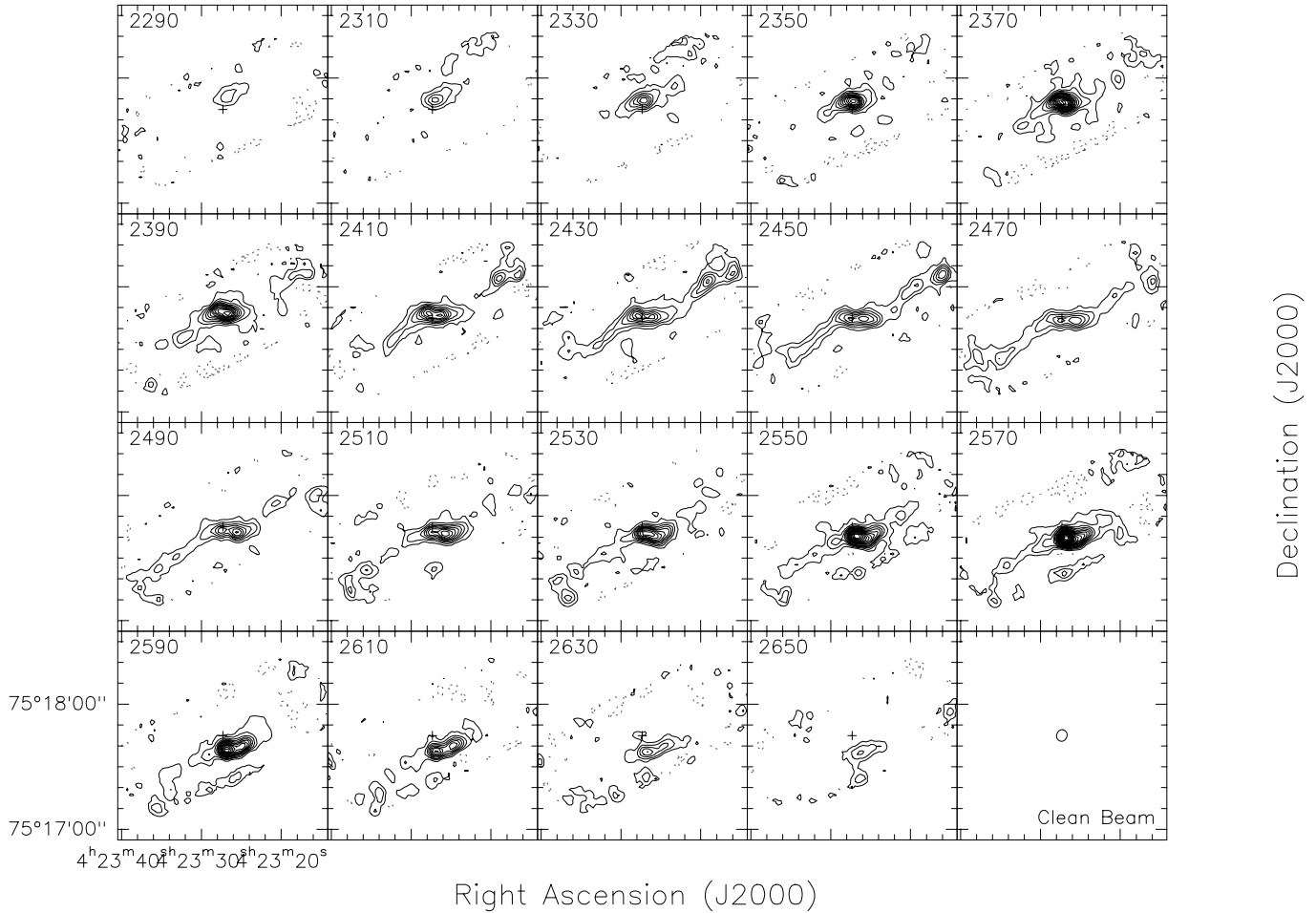


Fig. 2. CO(1–0) along the bar of NGC 1530 in 20 km s^{-1} channels from the PdB+PV data. The contour level is 30 mJy beam^{-1} . The clean beam is $5''.6 \times 5''.0$.

tral plateau has the same Z shape, the eastern lane is rather weak and regular, the western lane is very irregular with intense and compact clumps. We compared the ratio R of CO intensity to the dust optical depth. In a simple model, one expects the dust opacity in the visible to vary in the same way as the CO emission since the molecular gas and the dust are spatially associated. This seems to be true in the bar of NGC 1530, but the ratio R is not uniform. Regan et al. (1995) report $R \simeq 10 \text{ Jy beam}^{-1} \text{ km s}^{-1} \text{ A}_V^{-1}$ in the central plateau and $R \leq 4 \text{ Jy beam}^{-1} \text{ km s}^{-1} \text{ A}_V^{-1}$ in the western lane. Our CO map, with a slightly different beam ($5''.3$ instead of $4''.8$) gives for the central plateau $R \simeq 12 \text{ Jy beam}^{-1} \text{ km s}^{-1} \text{ A}_V^{-1}$ and for the west lane $R \simeq 7.5 \text{ Jy beam}^{-1} \text{ km s}^{-1} \text{ A}_V^{-1}$. That is, we find the difference between the central plateau and the extended lanes to be smaller than reported by Regan et al. (1995). The cloud $20''$ south of the center of NGC 1530 has $R \simeq 2.4 \text{ Jy beam}^{-1} \text{ km s}^{-1} \text{ A}_V^{-1}$, which is a much lower value than for the other clouds in the bar of NGC 1530. The CO emissivity changes possibly because of differences in kinetic temperature between the on-bar and off-bar clouds.

5. Kinematic and star formation

The CO lanes associated with the dust lanes are probably the sites of compression of the interstellar gas due to a shock wave. The density wave theory applied to the gas in barred potentials (Roberts et al. 1979) shows that along the bar, two leading shock fronts form, similar to the shock fronts associated with the spiral arms of galactic disks. These shock fronts are rectilinear in the case of strongly barred potentials (Athanasoula 1992). In these hydrodynamic models, and in a reference frame rotating with the bar, in which the shock fronts are stationary, the pre-shock gas flows outward, while the post-shock gas flows inward, toward the center of the galaxy. We now discuss the kinematics of the molecular gas along the bar of NGC 1530 and compare the observations with the predictions of hydrodynamic models. We then discuss possible correlations between the intensity of the shock wave and the rate of star formation along the bar.

5.1. Kinematic analysis

To study the compressed layer of gas in the transition between the pre-shock and the post-shock regime, we examined the ve-

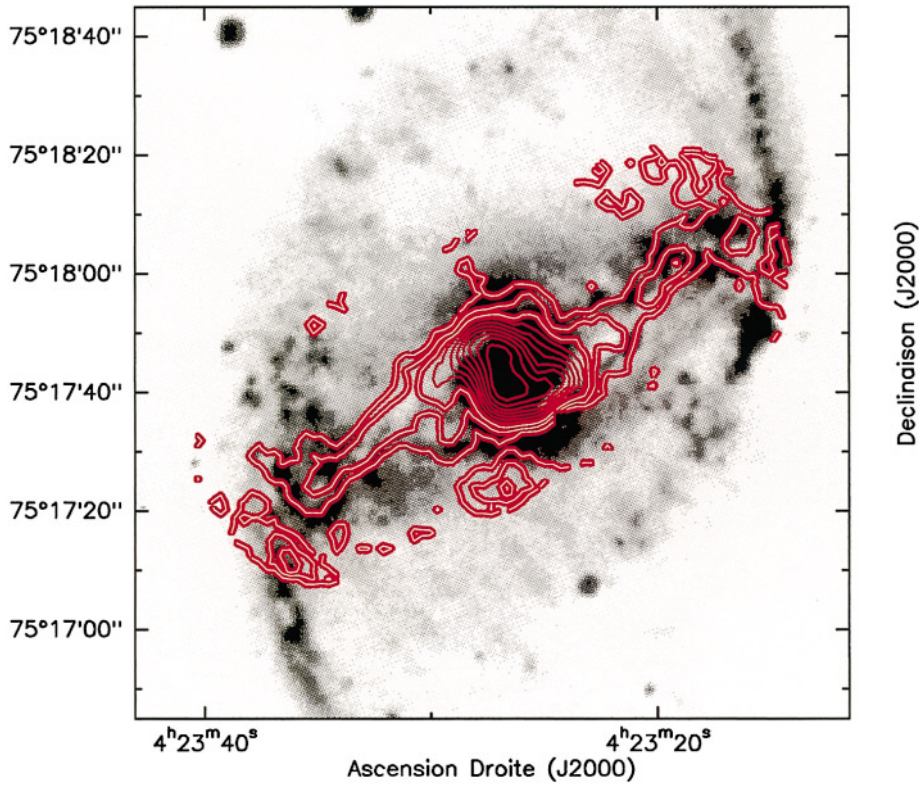


Fig. 3. Combined interferometer and single-dish map of NGC 1530 in CO (red contour levels of $4 \text{ Jy beam}^{-1} \text{ km s}^{-1}$), superimposed on an optical image of the bar and the beginning of the spiral arms (optical image NOAO).

locity distribution of the gas with position-velocity diagrams perpendicular to the CO lanes, at a position angle of 42° . We chose points along the CO lanes where CO is well detected.

Fig. 4 shows some of the position-velocity diagrams along the east and west CO lanes. For each of these two lanes, we show four diagrams along the lane. We have indicated for each diagram the distance of this diagram (L) to the dynamical center of NGC 1530. For the diagrams which are the closest to the center ($|L| = 15''.6$, i.e., a distance of $\simeq 4$ kpc to the center), one observes the largest velocity gradients: for $L = 15''.6$, the LSR velocity varies by 200 km s^{-1} over $6''$, with diffuse emission over this total range of velocity. This strong velocity gradient is probably due to the proximity of the inner Lindblad resonance (ILR) at a radius of 1.2 kpc (Reynaud & Downes 1997). Near this resonance, there is continuous generation of shocks between orbits parallel and perpendicular to the bar (Athanasoula 1992). The diagrams at $L = 40''.3$ on the western side and at $L = -35''.1$ on the eastern side are at the ends of the CO lanes, at radii of $\simeq 15$ kpc. These diagrams do not show strong velocity gradients, but only one compact molecular cloud at the end of each lane, that is isolated in both position and velocity. The velocity varies with position along the molecular gas lanes: near the ILR, the shock wave induces a large velocity jump, whereas near the ends of the bar, this jump is very weak. Between these points, the amplitude of the jump decreases smoothly from the center outwards. The same feature can be noted on the $\text{H}\alpha$ velocity map of Regan et al. (1997).

To quantify these results, we calculated the velocity field at every point along the bar where CO emission is found. Because

we can measure only the velocity component along the line of sight, we adopted the following hypotheses about the velocity field.

- The position angle of the line of nodes of NGC 1530 was assumed to be $PA \simeq 5^\circ$ (east of north) and the inclination of the galaxy to be $i \simeq 55^\circ$, where $i = 0^\circ$ means face-on. These values for NGC 1530 come from our previous, higher-resolution analysis of the central part of the galaxy (Reynaud & Downes 1997). They are close to the parameters obtained on larger scales with measurements in HI and $\text{H}\alpha$ (e.g. Regan et al., 1996, give $PA \simeq 8^\circ \pm 1^\circ$ and $i \simeq 45^\circ \pm 5^\circ$).

- For the position of the dynamical center and its systemic velocity we took $\alpha_{2000} = 04^{\text{h}}23^{\text{m}}26^{\text{s}}.7$, $\delta_{2000} = 75^\circ 17' 44''.0$, and $v_{\text{sys}} \simeq 2472 \text{ km s}^{-1}$ (Reynaud & Downes 1997). The systemic velocity is relative to the LSR. The accuracy of these values is: $0.5''$ in position and 5 km s^{-1} in the systemic velocity.

- The spiral arms are assumed to be trailing: since the southern part of the line of nodes is receding and the northern part is approaching, the galaxy's closest side is the western one.

- We adopted the rotation curve given in Fig. 7 of Regan et al. (1996), from $\text{H}\alpha$ observations with $4''$ resolution in the whole disk of NGC 1530, correcting for our adopted inclination ($i = 55^\circ$). This curve shows the circular component of the velocity along the line of nodes. The circular component of the velocity is probably different when measured along the bar (p.a. 115°), which is nearly perpendicular to the line of nodes (p.a. 5°) because of the quasi elliptical orbits followed by the gas. In other galaxies, the maximum difference between the two rotation curves (perpendicular and along the bar) is typically 100 to

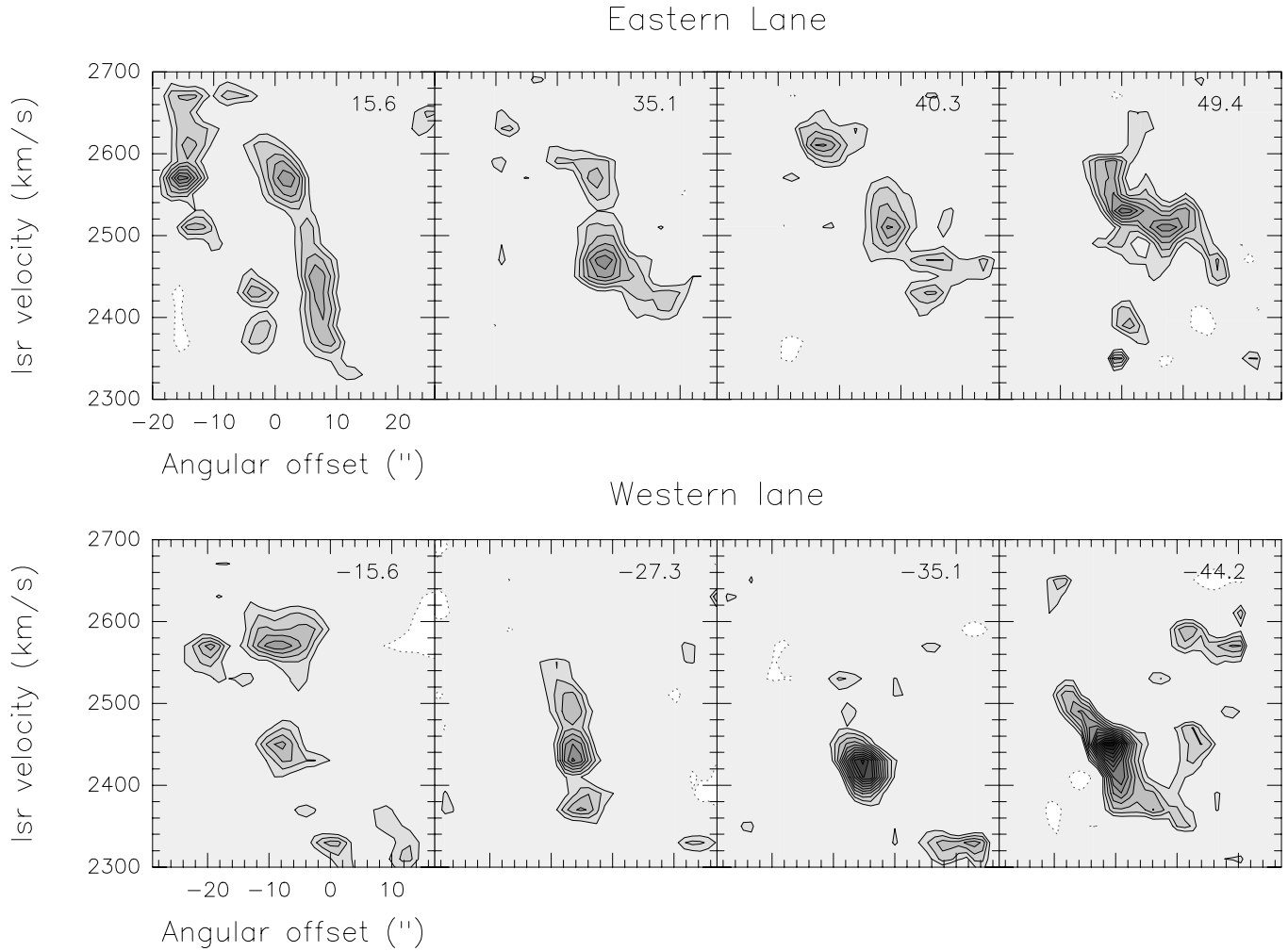


Fig. 4. Position-Velocity diagrams perpendicular to the CO lane of NGC 1530, at position angle 42° . Numbers in the upper-right corner of each diagram are the distance to the dynamical center (arcsec).

150 km s^{-1} (Duval & Athanassoula 1983). We consider this to be a possible systematic error in the rotation curve used here.

From position-velocity diagrams like those in Fig. 4, we isolated 29 clouds (19 in the east CO lane and 10 in the west lane). We noted each cloud's LSR velocity, v_{obs} , and position (r, θ) in the galactic plane, and then calculated the circular velocity of the cloud from the rotation curve, $v_{\text{rot}}(r)$. We deduced the radial component of the velocity from the formula :

$$|v_{\text{exp}}| = \left| \frac{v_{\text{obs}} - (v_{\text{sys}} - v_{\text{rot}} \sin i \cos \theta)}{\sin i \sin \theta} \right|$$

We adopted the following convention for the sign : $v_{\text{exp}} > 0$ for outward motions, $v_{\text{exp}} < 0$ for inward motions. We obtained the sign of the motion from the sign of $(v_{\text{obs}} - (v_{\text{sys}} - v_{\text{rot}} \sin i \cos \theta))$. On the western side (with respect to the line of nodes of the galaxy), a positive value of this difference indicates an inward motion; a negative value indicates an outward motion. On the eastern side, the signs are reversed.

To these 29 clouds, we added 10 clouds in the central plateau from the higher resolution CO maps ($2''$) of Reynaud & Downes

(1997), and used the kinematic model in that paper to calculate the non-circular motions.

5.2. Results

The velocity components of these 39 clouds are given in Tables 1 and 2. The uncertainties in the tabulated velocities are estimated as follows. We estimated above that the systematic error in the circular velocity v_{rot} is about $\Delta v_{\text{rot}} \simeq 100 \text{ km s}^{-1}$. Other uncertainties are $\Delta i \simeq 5^\circ$, $\Delta \phi \simeq 5^\circ$ and $\Delta v_{\text{sys}} \simeq 5 \text{ km s}^{-1}$, $\Delta v_{\text{obs}} \simeq 20 \text{ km s}^{-1}$. For $L \simeq -27''.3$ (Table 2) and $\theta \simeq 285^\circ$, for example, this yields an uncertainty in the expansion velocity of $\Delta v_{\text{exp}} \simeq 80 \text{ km s}^{-1}$. The difference in expansion velocity is about 150 km s^{-1} between the pre-shock and the post-shock zone. Hence in spite of the various uncertainties and the possible systematic error in the circular velocity, we still have strong evidence for a change of sign at the crossing of the shock, from an outward motion before the shock to an inward motion inside and after the shock. The closer the cloud to the minor axis of the galaxy ($\theta = 90^\circ$), the more precise is the determination

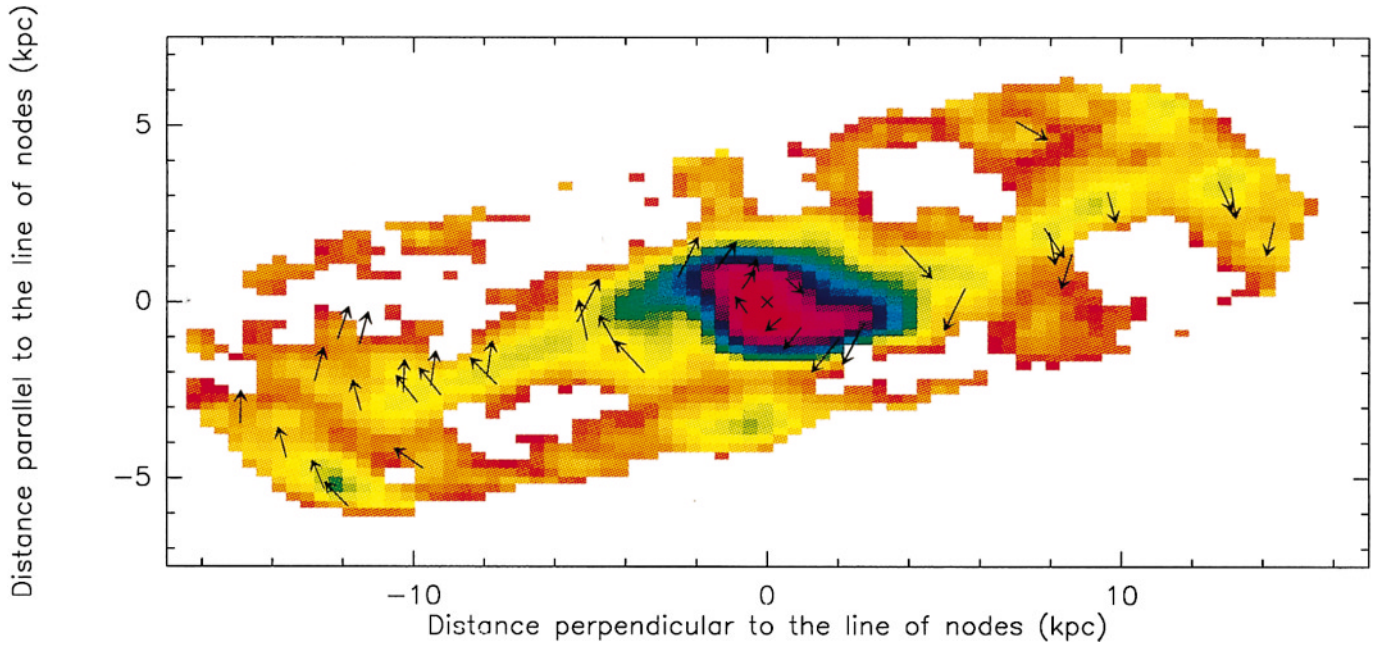


Fig. 5. Velocities of selected molecular clouds in the bar of NGC 1530 (arrows) superposed on a color map of CO integrated intensity.

Table 1. Kinematics of 39 clouds in the central plateau and along the bar of NGC 1530. Part I : **western plateau and CO lane.**

Radius kpc	θ deg	v_{obs} km s^{-1}	v_{rot} km s^{-1}	v_{exp} km s^{-1}	Remark
<i>western plateau</i>					
0.6	220	2550	115	0	Intense cloud.
0.85	321	2390	130	-4	Contact point of northern arc with nuclear zone.
1.2	233	2550	160	-2	Intense cloud.
2.3	243	2580	241	-55	southern Arc.
2.8	257	2550	250	-65	
<i>western lane</i>					
4.1	293	2330	241	90	$L = -15''.6$. Pre-shock cloud.
5.6	274	2570	230	-134	Very extended ($11''$) shock zone from pre-shock to post-shock; contains a cloud in circular rotation.
8.1	285	2380	190	65	$L = -27''.3$. Almost pointlike cloud; pre-shock.
8.2	284	2440	190	-10	Most intense cloud, pointlike, connected to the diffuse post-shock zone.
8.7	279	2520	185	-89	Post-shock.
8.7	306	2330	185	83	$L = -35''.1$. Weak and diffuse cloud.
10.1	288	2420	180	-8	Pointlike and intense cloud : extremity of CO lane.
13.2	285	2410	180	30	$L = -44''.2$. Extended zone; spiral arm.
13.5	284	2450	180	-17	Intense cloud.
14.5	279	2510	180	-74	Post-shock; beyond the bar.

θ is the azimuth of the cloud relative to the line of nodes in the plane of the galaxy.

of the expansion velocity, with the rotation component (which introduces most of the uncertainty) being cancelled.

Fig. 5 shows the velocity vectors (arrows) for the clouds listed in Tables 1 and 2. The arrows are understood to be in the galactic plane, with an arbitrary scaling factor adjusted for an

optimum visibility of the map. We have superposed on this field a face-on CO map of NGC 1530 in color levels. The map has been corrected for the 55° inclination of the galactic plane. Note that the sense of rotation of the gas in NGC 1530 is compatible with trailing spiral arms. In the following we will analyse in de-

Table 2. Kinematics of 39 clouds in the central plateau and along the bar of NGC 1530. Part II : **eastern plateau and CO lane.**

Radius kpc	θ deg	v_{obs} km s^{-1}	v_{rot} km s^{-1}	v_{exp} km s^{-1}	Remark
<i>eastern plateau</i>					
0.65	119	2520	115	12	Contact point of southern arc with nuclear zone.
0.8	62	2410	130	-16	Extended cloud.
0.8	44	2410	130	52	Edge of the extended cloud, toward northern arc.
1.7	57	2380	190	-10	Peak of the northern arc.
2.6	74	2390	245	-42	northern arc.
<i>eastern lane</i>					
4.0	120	2610	241	56	$L = 15''.6$. Diffuse emission with
4.4	109	2570	241	44	continuous pre-post shock sequence.
5.2	102	2510	233	0	Constant flux for $v_{\text{exp}} = 0$ to -150 km s^{-1} .
5.4	96	2370	230	-150	
8.0	107	2590	190	100	$L = 27''.3$. Continuous diffuse zone from pre-shock
					to shock (over $2'' \simeq 360 \text{ pc}$).
8.2	105	2450	190	-80	Flux peak.
9.6	106	2570	185	76	$L = 32''.5$. Pre-shock.
9.8	104	2450	185	-75	Flux peak. Shock; jump over $2''$.
11.6	96	2430	180	-70	Post-shock until $11'' \simeq 2 \text{ kpc}$.
10.3	106	2570	180	73	$L = 35''.1$. Pre-shock.
10.6	104	2470	180	-51	Flux peak. Shock.
12.2	95	2420	180	-80	Post-shock extended over 1.5kpc.
10.8	116	2610	180	100	$L = 40''.3$. Pre-shock at 1.2 kpc of the CO lane.
11.9	105	2510	180	0	Pointlike cloud. Extremity of the CO lane.
13.0	100	2430	180	-84	Post-shock pointlike cloud.
13.2	116	2580	180	60	$L = 49''.4$. Crossing of the spiral arm.
13.6	113	2530	180	0	Flux peak.
14.3	108	2510	180	-9	Intense cloud.
15.3	103	2470	180	-44	Weak cloud.

tail the behaviour of the gas across the CO lane, and the relation of this behaviour to the star formation rate along the bar.

5.3. Density wave and star formation

5.3.1. Density wave

Fig. 5 provides valuable information on the kinematics of the molecular gas from the inner parts of the galaxy toward the ends of the bar. Inside the central plateau, out to $\simeq 1.0 \text{ kpc}$ radius, circular rotation dominates, to within an accuracy of 10 km s^{-1} (r.m.s.) in the residuals (Reynaud & Downes 1997). Along the two bright arcs at the north-eastern and south-western edges of the central plateau (Fig. 1 of Reynaud & Downes 1997), there is a strong non-circular velocity component, in the inward direction. This non-circular component is also present all along the CO lanes, which are the continuation of the arcs of the plateau.

For the eastern lane our new data show that this non-circular component appears at $r \simeq 2 \text{ kpc}$, reaches a maximum at $\simeq 5.4 \text{ kpc}$ and then decreases progressively until it vanishes at the end of the CO lane, at $r \simeq 12 \text{ kpc}$, where the bar connects to the spiral arm. Our position-velocity diagrams show that the CO flux peaks in this inward-moving component, where it is two times stronger than in other velocity components. Upstream of this peak flux component (i.e. to the south for the eastern lane), we find the pre-shock zone with a weak CO emission and large

non-circular, outward motions (50 to 100 km s^{-1}). The flux of this outward-moving component is stronger near the galactic center. Downstream from the peak flux component (i.e. to the north for the eastern lane), one finds the post-shock zone with weak CO emission, increasing in strength at the end of the CO lane. The non-circular motions are inward in this zone (-70 to -150 km s^{-1}). The crossing of the CO lane corresponds to a velocity jump of 200 km s^{-1} in $2'' \simeq 400 \text{ pc}$ (Fig. 4). This velocity jump is a shear, because the direction of the shock front is almost parallel to the discontinuity in the velocity vector (Fig. 5). The amplitude of the velocity jump decreases from the beginning of the CO lane (close to the galactic center) out to its end (near the start of the spiral arm), where there is a cloud with a low velocity dispersion ($L = 40''.3$ in Fig. 4, $r = 11.9 \text{ kpc}$ in Table 2.)

The **western lane** shows the same characteristics as the eastern one, with a less regular CO distribution. The end of the lane is also occupied by a molecular cloud with a weak velocity dispersion, in pure circular rotation ($L = -35''.1$, $r = 10.1 \text{ kpc}$ in Table 1).

These observations can be compared with the predictions of hydrodynamic models such as those of Athanassoula (1992). Some of these isothermal models of the interstellar gas in barred potentials show the same gas distributions as are seen in early-type barred galaxies, when at least one inner Lindblad resonance is present. They show a central plateau with two intense arcs that

continue on, as two straight gas lanes until the ends of the bar, where there are strong concentrations of gas. The gas lane is associated with the shock feature, and shows inward motions of 100 km s^{-1} . Crossing the shock, the radial motion of the gas changes from outward (upstream) to inward (downstream) with a velocity difference of 250 km s^{-1} at a radius halfway to the ends of the bar. The velocity jumps are lower near the ends of the bar. In addition to the shear, the models predict a kinematic discontinuity through the shock in the azimuthal direction (see the model of Roberts et al. 1979). The resolution of the simulations, however, does not allow a separation of the shear and the shock (Athanasoula 1992).

Our CO observations roughly confirm this description. However, the asymmetry of the length of the bar (10 kpc west and 12 kpc east) and the differences in the structure between the two lanes are not features of any model, and probably are related to a mass distribution or dynamical history that is specific to NGC 1530.

5.3.2. Star formation

Fig. 6 shows the $\text{H}\alpha$ map of NGC 1530 at $4''$ resolution (Regan et al. 1996) superimposed on our CO map combining single-dish and interferometer data. This $\text{H}\alpha$ map is not corrected for extinction by dust. Inside the bar, the $\text{H}\alpha$ is concentrated in an intense nuclear disk and in some HII regions along the CO lanes and at the ends of the bar.

For the eastern lane, the $\text{H}\alpha$ intensity is almost zero close to the nuclear disk, then increases progressively along the lane, until the east end of the bar (region 5) where there is a local maximum (Fig. 6). The $\text{H}\alpha$ lane is slightly offset ($\simeq 5''$, or 900 pc) toward the downstream side of the CO lane. This offset vanishes near the end of the lane. This is as expected if the star formation traced by $\text{H}\alpha$ is due to the density wave that creates the CO lanes, with the corotation of this density wave near the end of the lanes (and near the ends of the bar).

The increasing $\text{H}\alpha$ emission with increasing radius along the bar is not an extinction effect, because the dust opacity increases towards the ends of the bar, according to the NIR and optical observations (Regan et al. 1995). The star formation rate clearly increases at the ends of the bar. However, the amount of available molecular gas is uniform along the lane, since the CO emission is uniform (provided the CO luminosity-gas column density conversion factor is uniform). The star formation efficiency, as traced by the ratio of $\text{H}\alpha$ intensity to CO intensity, increases with the radius along the lane. Moreover, the shear and the shock in the gas due to the bar potential decreases with radius, and becomes zero at the end of the lane. Although star formation seems to occur in clouds collapsing after the passage of a density wave (see e.g. Vogel et al. 1988), some physical effect must inhibit star formation in the dust lane near the nucleus of NGC 1530. We think the star formation efficiency probably decreases when, on a global scale, the amplitudes of the shear and the shock are too strong. On a small scale (scale size of individual clouds), this means that the relative velocity in cloud-cloud collisions is too high for the clouds to survive.

This effect is described by Tubbs (1982), who used numerical hydrodynamic simulations of barred galaxies (with no distinction between shock and shear) to test the role of physical parameters that control the contraction of gas in star forming complexes along the CO lanes. These parameters are the velocity of clouds entering the density wave and the pressure of the gas surrounding the clouds. In his simulations, Tubbs found that for velocities greater than a threshold between 20 and 60 km s^{-1} , the clouds are dispersed by the shock and do not contract.

Consider the distribution of HII regions in the eastern lane of NGC 1530. At a radius of $r = 5 \text{ kpc}$, the rotation velocity of the gas is $\simeq 233 \text{ km s}^{-1}$ and the rotation velocity of the density wave is $\Omega_p r$, with a pattern velocity of the bar $\Omega_p = 180 \text{ km s}^{-1}/14 \text{ kpc} = 13 \text{ km s}^{-1} \text{ kpc}^{-1}$, since the rotation velocity of the gas is 180 km s^{-1} at the corotation radius $r = 14 \text{ kpc}$ (1.2 times the 12 kpc radius of the bar, see Downes et al. 1996, or Regan et al. 1996 with another inclination angle). We therefore derive a velocity of $\Omega_p r \simeq 68 \text{ km s}^{-1}$ for the density wave at a radius of $r = 5 \text{ kpc}$. The molecular clouds thus enter the density wave with a velocity of $\simeq 165 \text{ km s}^{-1}$. From the same reasoning, at a radius of 8 kpc the entering velocity is 86 km s^{-1} . The $\text{H}\alpha$ map shows clearly that the star formation is weak at a radius of 5 kpc and intense at a radius of 8 kpc. If the entering velocity of the clouds constrains the star formation, then our observations suggest the existence of a velocity threshold between 80 and 170 km s^{-1} . At present, we cannot say which factor is more relevant for inhibiting the star formation, the shear or the shock.

An upper limit on the star formation time scale can be estimated from the distance between the density wave and the HII regions. At $r = 5 \text{ kpc}$, the distance between the CO and $\text{H}\alpha$ lanes is $\simeq 900 \text{ pc}$, with a speed of the clouds relative to the density wave of 165 km s^{-1} . This implies the OB stars formed less than 6×10^6 years after the passage of the density wave.

For the western lane, the situation is more confusing. There is no regular $\text{H}\alpha$ lane, but several HII regions along the CO lane (numbers 4, 6 and 7 in Fig. 6). Region 4 coincides with the end of the western CO lane, region 7 is downstream and close to the CO lane, and region 6 is devoid of CO emission, upstream and far away ($\simeq 2 \text{ kpc}$) from the CO lane. Region 4 corresponds to the usual HII region typically found at the end of the bar in early-type barred galaxies, the equivalent to region 5 at the end of the eastern lane. The HII region 7 is probably induced by the density wave traced by the CO lane, because it is near a strong peak in the optical opacity (Regan et al 1995), indicating a strong concentration of dust. However, the strong $\text{H}\alpha$ intensity at region 7 is surprising in comparison with the weak $\text{H}\alpha$ emission at the same radius in the eastern lane. The pressures of the intercloud medium on the dense clouds at the entrance of the shock lane are probably quite different, leading to large differences in star formation efficiency. Region 6, unlike region 7, has probably not been created by the density wave associated with the CO lane. This HII region does not correspond to any detected gas concentration. There is probably some gas associated with this star forming region, since the optical opacity peaks here (Regan et al. 1995), indicating the

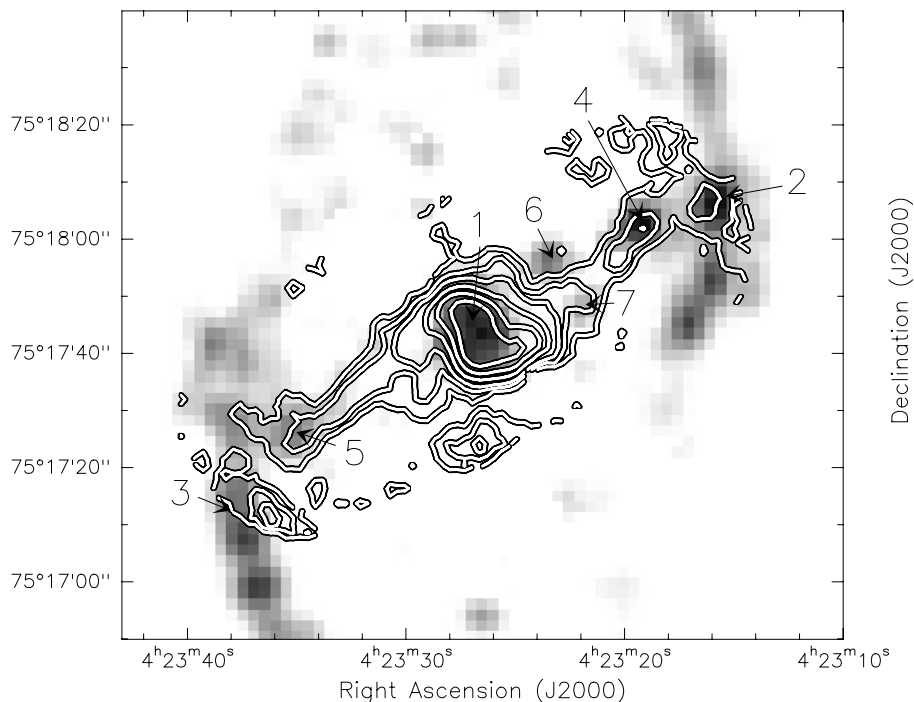


Fig. 6. Integrated H α map of NGC 1530 (greyscale; Regan et al. 1996) superposed on our CO map from combined interferometer and single-dish data (contour levels: 4, 8, 12, 20, 28, 36 Jy beam $^{-1}$ km s $^{-1}$). Numbers labelling the HII regions are from Regan et al. (1996).

presence of dust. This gas may be too cold or too diffuse to be detected in CO.

We also detect the opposite of region 6 : a cloud detected in CO and in the map of optical opacities, but showing no trace of star formation. Located 20'' south of the dynamical center (Fig. 6), well away from the shock waves, it appears to be stable against the fragmentation into the dense cores that are necessary to form stars.

6. Conclusion

We have studied in detail the behaviour of the molecular gas along the bar of NGC 1530. The bar has created offset shocks that provoke the inward streaming of gas toward the center of the galaxy. All along the gas and dust lanes, we detect strong velocity gradients that become weaker with increasing distance from the central plateau out to the ends of the bar. These gradients are produced by shocks in the gas. They correspond to an outward motion upstream of the shock and an inward motion inside of, and downstream of the shock. We compare these results with the predictions of hydrodynamic models, and find general agreement, particularly in the directions of the motions and the magnitude of the velocity jumps.

Our comparison of the gas kinematics with the sites of star formation indicates that intense shocks with velocity jumps > 100 km s $^{-1}$ between the upstream region and the shock, and that are associated with a large shear, inhibit the star formation by destroying the giant molecular cloud complexes.

Acknowledgements. We thank the technical staff of the 30m telescope for help during observations. We thank Dr. M. Regan for making available his H α map, and the referee for helpful comments.

References

- Athanassoula E., 1992, MNRAS 259, 345.
- Clark B.G., 1980, A & A 89, 377
- Combes F., 1988, in Galactic and Extragalactic Star Formation, eds. R.E. Pudritz and M. Fich (Dordrecht:Kluwer) 475
- Condon J.J., Helou G., Sanders D.B., Soifer B.T., 1996, ApJS 103, 81
- Downes D., Reynaud D., Solomon P.M., Radford S.J.E., 1996, ApJ 461, 186
- Friedli D., Benz W., 1993, A & A 268, 65
- Pence W.D., Blackman C.P., 1984, MNRAS 207, 9
- Phillips A.C., 1996, in Barred Galaxies, ASP Conference Series, vol. 91, 1996, eds. Buta, Crocker, Elmegreen, 44
- Regan M.W., Vogel S.N., Teuben P.J., 1995, ApJ 449, 576
- Regan M.W., Teuben P.J., Vogel S.N., van der Hulst T., 1996, AJ 112, 2549
- Regan, M. W., Vogel, S.N., Teuben, P. J., 1997, ApJ 482, L143
- Reynaud D., Downes D., 1997, A & A 319, 737
- Roberts V.W., Huntley J.M., van Albada G.D., 1979, ApJ 233, 67
- Tubbs A.D., 1982, ApJ 255, 458
- Viallefond F., Guilleaume S., Gueth F., 1994, IRAM internal Report
- Vogel S.N., Kulkarni S.R., Scoville N.Z., 1988, Nature, 334, 402